J|A|C|S ARTICLES

Published on Web 01/21/2009

Templated Nanocrystal-Based Porous TiO_2 Films for Next-Generation Electrochemical Capacitors

Torsten Brezesinski,*,† John Wang,‡,⊥ Julien Polleux,‡ Bruce Dunn,*,‡,§ and Sarah H. Tolbert*,†,§

Department of Chemistry and Biochemistry, University of California at Los Angeles, California 90095-1569, Department of Materials Science and Engineering, University of California at Los Angeles, California 90095-1595, and The California NanoSystems Institute, University of California at Los Angeles, California 90095

Received July 22, 2008; E-mail: tolbert@chem.ucla.edu; bdunn@ucla.edu; torsten.brezesinski@phys.chemie.uni-giessen.de

Abstract: The advantages in using nanoscale materials for electrochemical energy storage are generally attributed to short diffusion path lengths for both electronic and lithium ion transport. Here, we consider another contribution, namely the charge storage from faradaic processes occurring at the surface, referred to as pseudocapacitive effect. This paper describes the synthesis and pseudocapacitive characteristics of block copolymer templated anatase TiO_2 thin films synthesized using either sol−gel reagents or preformed nanocrystals as building blocks. Both materials are highly crystalline and have large surface areas; however, the structure of the porosity is not identical. The different titania systems are characterized by a combination of small- and wide-angle X-ray diffraction/scattering, combined with SEM imaging and physisorption measurements. Following our previously reported approach, we are able to use the voltammetric sweep rate dependence to determine quantitatively the capacitive contribution to the current response. Considerable enhancement of the electrochemical properties results when the films are both made from nanocrystals and mesoporous. Such materials show high levels of capacitive charge storage and high insertion capacities. By contrast, when mesoscale porosity is created in a material with dense walls (rather than porous walls derived from the aggregation of nanocrystals), insertion capacities comparable to templated nanocrystal films can be achieved, but the capacitance is much lower. The results presented here illustrate the importance of pseudocapacitive behavior that develops in high surface area mesoporous oxide films. Such systems provide a new class of pseudocapacitive materials, which offer increased charge storage without compromising charge storage kinetics.

Introduction

Capacitive energy storage has been somewhat overlooked as an energy storage technology. It is based on electrochemical capacitors (ECs), which include double-layer capacitors (also termed supercapacitors or ultracapacitors) and pseudocapacitors.[1−5] These energy storage devices are related to batteries but have different storage mechanisms. Capacitive storage offers a number of desirable properties, including charging within seconds, long-term cycling stability, and the ability to deliver up to 10 times more power than batteries. Moreover, it is apparent that there are unique opportunities for ECs, such as in energy recovery where batteries are simply not appropriate. The limiting feature that prevents more widespread usage of ECs has been the relatively low energy density of the materials employed in capacitive storage applications. Currently, the field is largely based on materials made of carbon and electric double-layer storage processes.[6−8] In this work, we present methods to overcome the limitations of ECs through the use of nanoporous transition metal oxides. Such materials allow for charge capacities comparable to those found in batteries without compromising high charging/discharging rates.

A significant feature occurs as electroactive materials approach nanoscale dimensions. The charge storage of cations from faradaic processes occurring at the surface (cations electrochemically adsorb onto the surface through charge-transfer processes), referred to as pseudocapacitive effect,[9] becomes increasingly important.[3,10] In recent work,[11] Dunn et al. used a detailed cyclic voltammetric analysis to establish

† Department of Chemistry and Biochemistry.
‡ Department of Materials Science and Engineering.
§ The California NanoSystems Institute.
⊥ Current address: HRL Laboratories, LLC, Malibu, CA 90265.

(1) Winter, M.; Brodd, R. J. *Chem. Rev.* **2004**, *104*, 4245–4269.
(2) Arico, A. S.; Bruce, P.; Scrosati, B.; Tarascon, J. M.; Van Schalkwijk, W. *Nat. Mater.* **2005**, *4*, 366–377.
(3) Jamnik, J.; Maier, J. *Phys. Chem. Chem. Phys.* **2003**, *5*, 5215–5220.
(4) Bruce, P.; Scrosati, B.; Tarascon, J. M. *Angew. Chem., Int. Ed.* **2008**, *47*, 2930–2946.
(5) Conway, B. E. *Electrochemical Supercapacitors*; Kluwer Academic: New York, 1999.
(6) Frackowiak, E.; Beguin, F. *Carbon* **2001**, *39*, 937–950.
(7) Chmiola, J.; Yushin, G.; Gogotsi, Y.; Portet, C.; Simon, P.; Taberna, P. L. *Science* **2006**, *313*, 1760–1763.
(8) Emmenegger, C.; Mauron, P.; Sudan, P.; Wenger, P.; Hermann, V.; Gallay, R.; Zuttel, A. *J. Power Sources* **2003**, *124*, 321–329.
(9) Conway, B. E.; Birss, V.; Wojtowicz, J. *J. Power Sources* **1997**, *66*, 1–14.
(10) Balaya, P.; Bhattacharyya, A. J.; Jamnik, J.; Zhukovskii, Y. F.; Kotomin, E. A.; Maier, J. *J. Power Sources* **2006**, *159*, 171–178.
(11) Wang, J.; Polleux, J.; Lim, J.; Dunn, B. *J. Phys. Chem. C* **2007**, *111*, 14925–14931.

10.1021/ja8057309 CCC: $40.75

quantitatively the dependence of the pseudocapacitance on the particle size of anatase TiO_2 nanocrystals. The results showed that the pseudocapacitive contribution to charge storage increases significantly for particle sizes <10 nm, leading to higher levels of total stored charge and much faster charge/discharge kinetics.

While these results are exciting, capacitive energy storage in bulk nanoparticle films is hindered by slow molecular transport of solvent and ions through the network. To address this problem, we turn to films with three-dimensionally interconnected porosity. Such thin film materials can be readily formed by coassembly of inorganic oligomers with structure-directing agents using an evaporation induced self-assembly (EISA) process.[12−15] In recent years, it has been shown that a broad range of inorganics possess the potential for crystalline grains while retaining nanoscale order.[16−21] However, the majority of these self-organized materials feature only a semicrystalline or even amorphous pore wall structure which makes them unsuitable for most applications. The lack of control over crystallization and the associated stress that crystallization builds into the material is one of the major weaknesses of this approach (the loss of periodicity is often faster than the rate of crystallization).

Polymer-directed assembly of preformed nanocrystals into three-dimensional architectures is an alternative route to circumvent loss of periodicity/porosity upon crystallization.[22−26] The synthesis of nanocrystalline building blocks with well-defined size (<10 nm) and shape, low polydispersity, and good redispersability is complicated, though. Thus, only a few well-defined materials (mainly in the form of powders) with nanoscale periodicity made from preformed nanocrystals have been reported up until now, such as ceria (CeO_2)[24,25] or tin oxide (SnO_2).[26]

Here, we report the synthesis and characterization of polymer-templated sol−gel and nanocrystal-based anatase TiO_2 thin films. Both materials have a highly crystalline pore−solid architecture and a large surface area. Despite using the same template for each material, however, the structure of the porosity is not identical. We next examine the redox processes present in these materials and show that high capacitive charge storage can be achieved for the mesoporous films produced using preformed nanocrystals. Overall, the results presented in this work represent a concrete design template for the synthesis of redox active materials optimized for capacitive energy storage.

Experimental Section

Materials. $TiCl_4$ (99.9%) and anhydrous benzyl alcohol (99.8%) were purchased from Sigma-Aldrich. $H(CH_2CH_2CH_2(CH)CH_2CH_3)_{89}(OCH_2CH_2)_{79}OH$ (referred to as KLE22) and $H(CH_2CH(CHCH_2))_{310}(OCH_2CH_2)_{560}OH$ (referred to as KLE23) were used as organic templates.[27]

Synthesis of Anatase TiO_2 Nanocrystals. In a water-free container, 0.5 mL of $TiCl_4$ is slowly added to 2 mL of EtOH and then combined with 10 mL of anhydrous benzyl alcohol. The container is loosely sealed and the sol heated at 80 °C for 9 h. To isolate the nanocrystalline particles, 1 mL of the suspension is precipitated in 12 mL of diethyl ether and centrifuged at 5000 rpm. The obtained white powder is then dispersed in 3 mL of EtOH and sonicated for 2 h, yielding a transparent sol.[11,18]

Synthesis of Mesoporous Sol−Gel Type Films. First, 600 mg of $TiCl_4$ is carefully combined with 3 mL of EtOH. After 10 min, 100 mg of KLE22 dissolved in 3 mL of EtOH and 0.5 mL of double distilled H_2O is added. Thin films are produced via dip-coating on polar substrates. Optimal conditions include 20% relative humidity and a constant withdrawal rate of 1−10 mm/s. The films need to be aged at 300 °C for 12 h prior to template removal to prevent loss of mesoscale order over the course of crystallization. For best results, films are calcined using a 1 h ramp to 600 °C, followed by a 10 min soak.

Synthesis of Mesoporous Nanocrystal-Based Films. 60 mg of either KLE22 or KLE23 dissolved in 0.5 mL of EtOH is added to 4 mL of the anatase nanoparticle sol (content: 15 mg/mL). Once the solution is homogeneous, 0.2 mL of double distilled H_2O is added. Thin films are produced via dip-coating at 30% relative humidity. Calcination of the composite to fully remove the polymer template is done using a 2 h ramp up to 600 °C, followed by a 1 h soak. Untemplated nanocrystal-based films are produced without any template but under otherwise identical conditions. The thickness of a templated film is only about 150 nm (as-synthesized) due to the relatively low TiO_2 nanoparticle content in the sol. However, multiple dip-coating is a possibility to get film thicknesses of >500 nm.

Methods. TEM was performed using a JEOL model 2000FX electron microscope operating at 200 kV. Tapping mode AFM images were acquired with a multimode AFM from Vecco Instruments employing Olympus microcantilevers (resonance frequency: 300 kHz, force constant: 42 N/m). FESEM was performed using a JEOL model 6700F electron microscope.

WAXD measurements were carried out on a D8-GADDS diffractometer from Bruker instruments (Cu Kα radiation), as well as on an XPert PRO MPD diffractometer from Panalytical instruments. 2D-SAXS patterns were collected on Beamline 1-4 at the Stanford Synchrotron Radiation Laboratory and on a Nonius rotating anode with MAR CCD area detector (sample−detector distance: 750 mm). XPS spectra were acquired on a Physical Electronics ESCA 5600 spectrometer with monochromatic Al Kα X-ray source (power: 200 W/14 kV) and a multichannel detector OmniIV. The electron takeoff angle θ to the sample surface was adjusted to 45°. The adventitious hydrocarbon C1s signal at 284.6 eV was used as the energy reference to correct for charging.

Toluene physisorption measurements were performed with a QCM device. A 10 MHz QCM device was utilized to measure frequency changes. The partial pressures were calculated using the van der Waals equation with real gas-state assumptions (van der Waals parameters for toluene: $a = 24.86$, $b = 0.1497$). The film thickness was determined with a Vecco Dektak 6 M profilometer.

Electrochemical experiments were carried out in a three-electrode cell using a PAR EG&G 273 potentiostat. The working electrode

(12) Ogawa, M. *Langmuir* **1997**, *13*, 1853–1855.
(13) Brinker, C. J.; Lu, Y. F.; Sellinger, A.; Fan, H. Y. *Adv. Mater.* **1999**, *11*, 579–585.
(14) Zhao, D. Y.; Feng, J. L.; Huo, Q. S.; Melosh, N.; Fredrickson, G. H.; Chmelka, B. F.; Stucky, G. D. *Science* **1998**, *279*, 548–552.
(15) Goltner, C. G.; Antonietti, M. *Adv. Mater.* **1997**, *9*, 431–436.
(16) Brezesinski, T.; Groenewolt, M.; Antonietti, M.; Smarsly, B. *Angew. Chem., Int. Ed.* **2006**, *45*, 781–785.
(17) Sun, D.; Riley, A. E.; Cadby, A. J.; Richman, E. K.; Korlann, S. D.; Tolbert, S. H. *Nature* **2006**, *441*, 1126–1130.
(18) Brezesinski, T.; Groenewolt, M.; Amenitsch, H.; Antonietti, M.; Smarsly, B. *Adv. Mater.* **2006**, *18*, 1827–1831.
(19) Smarsly, B.; Antonietti, M. *Eur. J. Inorg. Chem.* **2006**, *6*, 1111–1119.
(20) Brezesinski, T.; Antonietti, M.; Smarsly, B. *Adv. Mater.* **2007**, *19*, 1074–1078.
(21) Choi, S. Y.; Mamak, M.; Speakman, S.; Chopra, N.; Ozin, G. A. *Small* **2005**, *1*, 226–232.
(22) Antonietti, M.; Niederberger, M.; Smarsly, B. *Dalton Trans.* **2008**, *1*, 18–24.
(23) Bosc, F.; Ayral, A.; Albouy, P. A.; Guizard, C. *Chem. Mater.* **2003**, *15*, 2463–2468.
(24) Corma, A.; Atienzar, P.; Garcia, H.; Chane-Ching, J. Y. *Nat. Mater.* **2004**, *3*, 394–397.
(25) Deshpande, A. S.; Pinna, N.; Smarsly, B.; Antonietti, M.; Niederberger, M. *Small* **2005**, *1*, 313–316.
(26) Ba, J. H.; Polleux, J.; Antonietti, M.; Niederberger, M. *Adv. Mater.* **2005**, *17*, 2509–2512.
(27) Thomas, A.; Schlaad, H.; Smarsly, B.; Antonietti, M. *Langmuir* **2003**, *19*, 4455–4459.

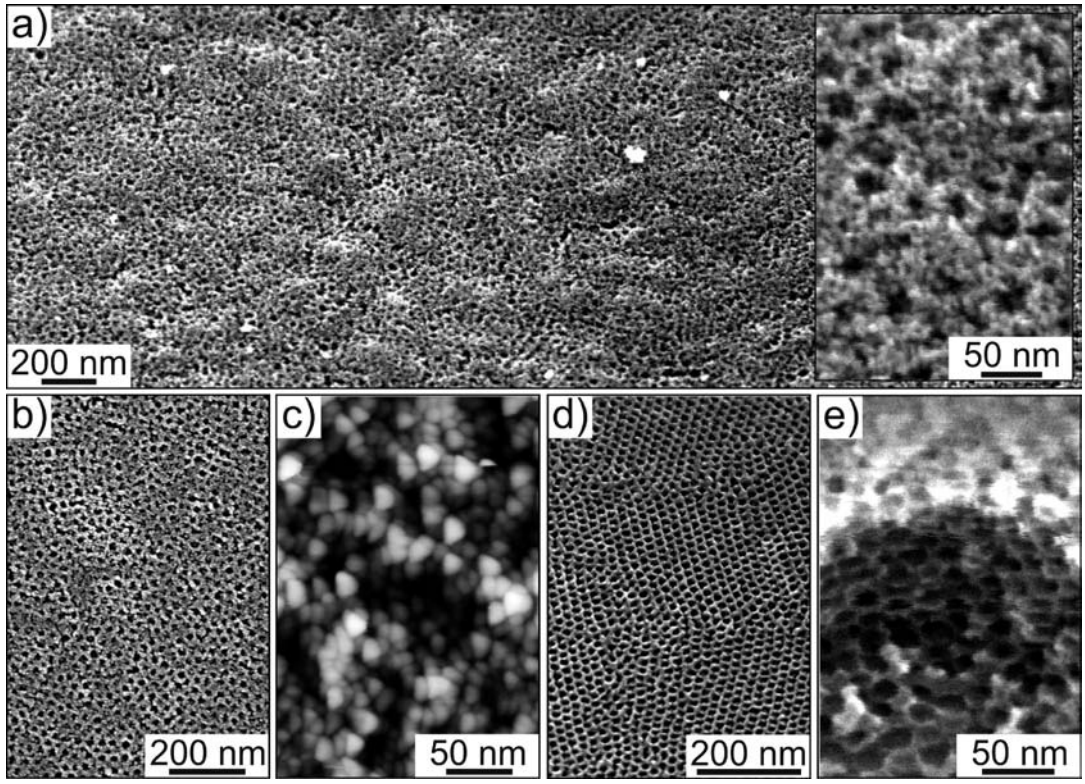

Figure 1. Nanoscale structure of self-organized anatase TiO_2 thin films. (a−b) Low-magnification top-view FESEM images of KLE23- (a) and KLE22-templated (b) nanocrystal films. The inset in (a) shows a high-magnification top-view FESEM image; the porosity is bimodal with 1−4 and 20−25 nm diameter pores. (c) Tapping mode AFM image of a KLE23-templated nanocrystal film calcined at 900 °C. (d−e) FESEM images of a KLE22-templated sol−gel film held at a tilt of 45°. (d) Top surface. (e) Cross section.

was ITO glass upon which the TiO_2 films were deposited. A lithium foil several times the area of the working electrode was used as the counter electrode; the reference electrode was a lithium wire. The electrolyte solution was 1.0 M $LiClO_4$ in propylene carbonate (PC). All measurements were performed in an argon-filled glovebox using cutoff voltages at 2.5 and 1.5 V vs Li/Li^+.

Results and Discussion

Nanoscale Structure. To produce nanocrystalline TiO_2 building blocks, a facile surfactant-free synthesis in benzyl alcohol was used.[28] Postfunctionalization of these nanoparticles was not necessary to achieve a sufficient redispersability in $EtOH/H_2O$ (up to 20 mg/ml) or to prevent particle agglomeration (see TEM image in Supporting Information, Figure S1). According to wide-angle X-ray diffraction (WAXD, Figure 3b, inset), the as-synthesized nanoparticles are crystalline with an average grain size of 4−5 nm (obtained from Scherrer analysis of the peak widths). Identification of the main peaks and relative intensities was found to match the anatase titania phase according to JCPDS reference card no. 21-1272.

For the synthesis of films with three-dimensionally interconnected porosity, an ethanolic solution containing either a molecular precursor, such as tetraethyl orthotitanate, or preformed nanocrystals and an organic template is spin- or dip-coated onto a polar substrate. Upon evaporation, the system coassembles to form a mesostructured inorganic/organic composite. This composite is then made porous by removing the template to leave a pore−solid architecture. In this work, we used KLE block copolymers (poly(ethylene-*co*-butylene)-*block*-poly(ethylene oxide), which have been shown to possess many desirable templating properties, including high thermal stability and a strong tendency to form ordered structures in a broad range of solvents.[27] These block copolymers thus are highly suitable for synthesizing ordered large-pore metal oxide films with crystalline pore walls.[16−21,29]

Figure 1a−b presents top-view field-emission scanning electron microscope (FESEM) images obtained from self-organized nanocrystal-based TiO_2 films after complete removal of the KLE template at 600 °C. Both images show disordered, but macroscopically homogeneous architectures with either 17−19 (KLE22-templated) or 20−25 nm diameter pores (KLE23-templated). These films are crack-free, and more importantly, the pores at the surface are open. Figure 1a further presents a higher-magnification top-view FESEM image, which reveals a bimodal structure with 1−4 nm diameter pores located between larger KLE-derived mesopores. We assume that the sub-4 nm pores result from a combination of random nanocrystal aggregation during synthesis and the fact that the surfaces are initially covered with benzyl alcohol ligands, which degrade during calcination. Also, the image shows that the pore walls (thickness of 15−25 nm) are comprised of several layers of nanocrystals. The fact that these nanocrystalline building blocks retain their individual identity and do not fuse at temperatures below 600 °C will become important in the following sections on capacitive charge storage. Single nanocrystals can also be observed with atomic force microscopy (AFM). Figure 1c shows a tapping mode AFM image of a templated nanocrystal film that had been thermally treated at 900 °C. In this case, however,

(28) Niederberger, M.; Bartl, M. H.; Stucky, G. D. *Chem. Mater.* **2002**, *14*, 4364–4370.

(29) Brezesinski, T.; Fattakhova-Rohlfing, D.; Sallard, S.; Antonietti, M.; Smarsly, B. *Small* **2006**, *2*, 1203–1211.

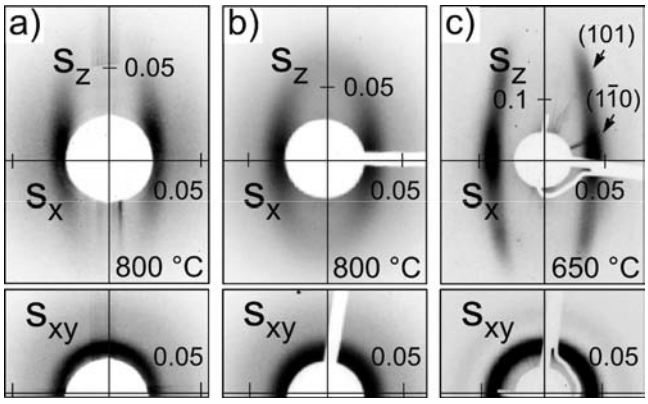

Figure 2. 2D-SAXS patterns of cubic mesoporous TiO_2 thin films. (a) KLE23-templated nanocrystal film. (b) KLE22-templated nanocrystal film. (c) KLE22-templated sol−gel film. The patterns were acquired at an angle of incidence $\beta = 7°$ (top) and 90° (bottom). Scattering vector s components are given in units of 1/nm; $s = 2/\lambda \sin \theta$.

the grain size is about 15 nm, which agrees well with WAXD data. It is important to note that similar syntheses using Pluronic type block copolymer templates (P123, F127, etc.) failed, a result that underscores the superior templating properties of the KLE block copolymers used in this work.

For comparison, Figure 1d−e shows FESEM images of a more standard KLE22-templated sol−gel TiO_2 film obtained after crystallization at 600 °C. The high quality lattice with ordered 14 nm diameter mesopores is characteristic of sol−gel-type oxide phases templated with the block copolymer KLE. In contrast to the nanocrystal-based titania systems, the synthesis produces films with a highly ordered cubic pore−solid architecture and an extremely flat air−solid interface (rms roughness of <0.5 nm). The fact that the KLE22-derived mesopores are smaller than the analogous pores in the nanocrystal films can be attributed to a strong interaction of the poly(ethylene oxide) corona chains with molecular precursors.

These results are further supported by two-dimensional small-angle X-ray scattering (2D-SAXS) data, which were collected on a laboratory rotating anode and on beamline 1-4 at the Stanford Synchrotron Radiation Laboratory. Thin films produced on ultrathin silicon substrates allow these measurements to be performed in both transmission and reflection mode. Figure 2 shows 2D-SAXS patterns for KLE-templated sol−gel and nanocrystal-based anatase TiO_2 thin films. For small angles of incidence (defined as the angle between the X-ray beam and the plane of the substrate), i.e., at $\beta < 10°$, the sol−gel films (Figure 2c) produce patterns with distinct maxima. These maxima can be indexed in terms of a body centered cubic (bcc) *Im3m*-derived pore system with (110) orientation relative to the plane of the substrate (lattice parameter $a = 34$ nm). The nanocrystal films (Figure 2a−b), by contrast, reveal only diffuse ellipsoidal rings with strong in-plane scattering maxima (KLE22-templated: d_{xy}-spacing of 35 nm, KLE23-templated: d_{xy}-spacing of 40 nm). This is characteristic of cubic pore structures featuring a higher degree of lattice distortions and a substantially lower degree of preferred orientation to the substrate.

The 2D-SAXS patterns further indicate anisotropic lattice contraction (perpendicular to the plane of the substrate). On the basis of the relative position of the out-of-plane reflections, a contraction of 50−60% was determined for both KLE-templated sol−gel and nanocrystal films. It might seem logical that the nanocrystal-based materials would show less contraction than the sol−gel films because the titania is already crystalline and

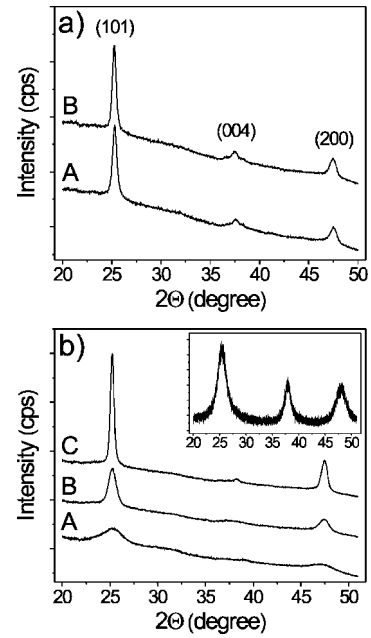

Figure 3. Temperature-dependent WAXD patterns of mesoporous anatase TiO_2 thin films. (a) KLE22-templated sol−gel film. (b) KLE22-templated nanocrystal film. The samples were subjected to annealing temperatures of 500 (A) and 700 °C (B) and 200 (A), 600 (B), and 900 °C (C), respectively. The inset in (b) shows a typical WAXD pattern of as-synthesized TiO_2 nanocrystals.

does not lose water upon heating. This is compensated by the fact that the nanocrystal-based materials contain significant organic material from the benzyl alcohol on the nanocrystal surfaces (15−20 wt.-% with respect to TiO_2 by thermogravimetric analysis). Like the water in traditional sol−gel films, this organic material is lost during heating, causing contraction of the film normal to the substrate. Patterns taken in transmission geometry, i.e., at $\beta = 90°$, show isotropic diffraction rings, which confirm the presence of randomly oriented (polycrystalline) domains parallel to the plane of the substrate. Moreover, 2D-SAXS demonstrates that the templated nanocrystal films can be heated up to temperatures as high as 900 °C before losing mesoscale order. To the best of our knowledge, this is the first example of a polymer-templated titania film that is able to withstand such temperatures.[30−33] In the sol−gel films, however, nanoscale periodicity is lost at much lower temperatures (ca. 700 °C) due to diffuse nanocrystal growth in the pore walls.

To study the crystallization behavior and to obtain detailed information about the grain size and growth, temperature-dependent WAXD measurements were conducted. Both types of films produce peaks characteristic of tetragonal anatase according to JCPDS reference card no. 21-1272 with no indications for either rutile or brookite phases. The crystallization of the templated sol−gel films occurs at around 500 °C (Figure 3a), leading to randomly oriented 13−14 nm nanocrystals in the pore walls. Interestingly, no significant grain growth is

(30) Smarsly, B.; Grosso, D.; Brezesinski, T.; Pinna, N.; Boissière, C.; Antonietti, M.; Sanchez, C. *Chem. Mater.* **2004**, *16*, 2948–2952.
(31) Grosso, D.; Soler-Illia, G. J. D. A.; Crepaldi, E. L.; Cagnol, F.; Sinturel, C.; Bourgeois, A.; Brunet-Bruneau, A.; Amenitsch, H.; Albouy, P. A.; Sanchez, C. *Chem. Mater.* **2003**, *15*, 4562–4570.
(32) Kirsch, B. L.; Richman, E. K.; Riley, A. E.; Tolbert, S. H. *J. Phys. Chem B* **2004**, *108*, 12698–12706.
(33) Choi, S. Y.; Lee, B.; Carew, D. B.; Mamak, M.; Peiris, F. C.; Speakman, S.; Chopra, N.; Ozin, G. A. *Adv. Funct. Mater.* **2006**, *16*, 1732–1738.

observed up to 700 °C, which explains the good thermal stability. These films can be considered as 100% crystalline after calcination at 600 °C.

The templated nanocrystal films, on the other hand, have already crystalline pore walls (ca. 4−5 nm grains) in the as-synthesized state (Figure 3b). In this case, the XRD data were fit with Gaussians to track the evolution of the (101) anatase peak as a function of temperature. At around 400 °C (the point where the organic ligands and the KLE template are combusted), the peak begins to grow at a moderate rate. The full width at half-maximum intensity decreases gradually with increasing temperature, which implies that the particle size can be readily adjusted. At 900 °C, the TiO_2 nanocrystals reach a "critical" size of about 15 nm, which agrees well with the pore wall thickness observed with FESEM. Higher temperatures (up to 1100 °C) lead to further grain growth but do not result in phase-transformation of the anatase lattice into rutile (impurities are known to facilitate this transition). This result suggests that these films are of high purity (see XPS data in Supporting Information, Figure S2). Moreover, WAXD (Figure 3) shows that for both templated sol−gel and nanocrystal films the pore walls are composed of crystallographically oriented nanocrystals. However, note that the degree of orientation is relatively low. In the case of sol−gel films, polarizability appears to be the crucial factor for the oriented nucleation and growth of anatase TiO_2; this arises as a consequence of the anisotropic distribution of atoms in the unit cell.[18] The domain orientation in nanocrystal-based films, however, is more likely attributed to oriented attachment of the preformed building blocks because of the different surface energies of anatase crystal faces.[34]

The porosity was analyzed using toluene physisorption based on gravimetric measurements with a quartz crystal microbalance (QCM) device and by ellipsometric porosimetry. Figure 4a−c shows typical adsorption−desorption isotherms for KLE23-templated and untemplated (i.e., formed without any diblock copolymer template) nanocrystal films, as well as for KLE22-templated sol−gel films. Both nanocrystal films were treated at 450 °C in oxygen for 1 h (higher temperatures would damage the quartz resonator), while the sol−gel-type film was calcined at 600 °C in air for 10 min. The shape of the isotherms (type IV) for all samples is characteristic of mesoporous materials. The pronounced hysteresis loop of the templated sol−gel film (Figure 4a) suggests that the mesopore cavities are interconnected through significantly smaller necks. In this case, the Brunauer−Emmett−Teller (BET) surface area was determined to be 180−200 m^2/g.

The toluene adsorption/desorption measurements for the KLE23-templated nanocrystal film corroborates the observations made from SEM that the films contain larger mesopores and smaller pores formed between the anatase nanocrystals. Both templated and untemplated nanocrystal films show a condensation step at relative pressures of 0.2−0.3, which can be unambiguously attributed to the sub-4 nm pores that are formed by random nanocrystal aggregation. The templated film further shows a hysteresis loop at higher relative pressures; the porosity is thus bimodal. The fact that the shape and width of the hysteresis loop is different compared to the sol−gel film can be ascribed to the different pore size and the broader pore size distribution (see Figure 1). The BET surface areas of KLE23-templated and untemplated nanocrystal films were determined

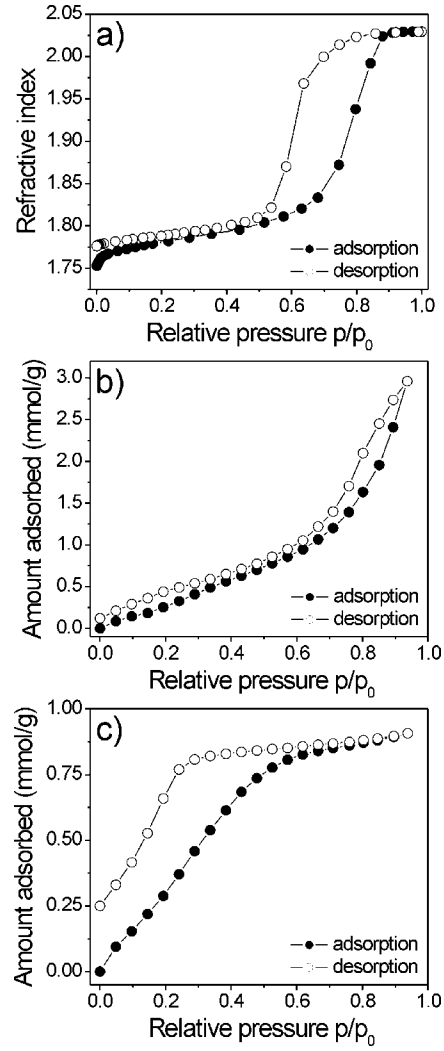

Figure 4. Toluene adsorption−desorption isotherms for self-organized TiO_2 thin films. (a) KLE22-templated sol−gel film, showing a more standard isotherm for sol−gel derived films with monomodal pore structure. (b) KLE23-templated nanocrystal film with bimodal porosity. (c) Untemplated nanocrystal film with sub-4 nm pores that are formed by random nanocrystal aggregation. The nanocrystal based films were calcined at 450 °C in oxygen and porosity was measured using gravimetric QCM, while the sol−gel-type film was calcined at 600 °C in air and porosity was measured using ellipsometric porosimetry.

to be 250−300 and 350−400 m^2/g, respectively. Overall, physisorption demonstrates that the polymer templated films employed in this work have open mesoscale architectures and that films formed from preformed anatase TiO_2 building blocks also contain smaller pores between the nanocrystals.

Electrochemical Properties. To examine the redox processes present in these materials, thin films were deposited on ITO-coated glass and calcined at 600 °C. According to X-ray diffraction, the sol−gel TiO_2 films contained 13−14 nm nanocrystals in the pore walls, while the nanocrystal-based films were comprised of 8 nm anatase particles.

Cyclic voltammetry (CV) was first used to analyze the charge storage behavior. Figure 5 shows typical cyclic voltammograms for KLE23-templated nanocrystal films at various sweep rates. The lithium insertion/extraction into/from anatase occurs at around 1.7 and 2.0 V vs Li/Li^+, respectively. This process can be expressed by

$$TiO_2 + xLi^+ + xe^- \leftrightarrow Li_xTiO_2 \quad (1)$$

(34) Niederberger, M.; Colfen, H. *Phys. Chem. Chem. Phys.* **2006**, *8*, 3271–3287.

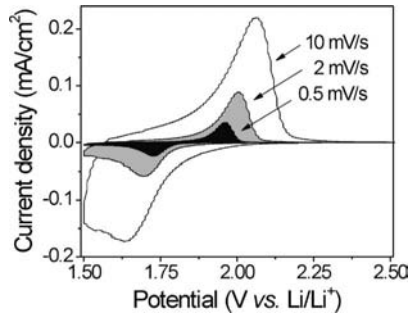

Figure 5. Typical cyclic voltammetric responses of KLE-templated nanocrystal films at various sweep rates.

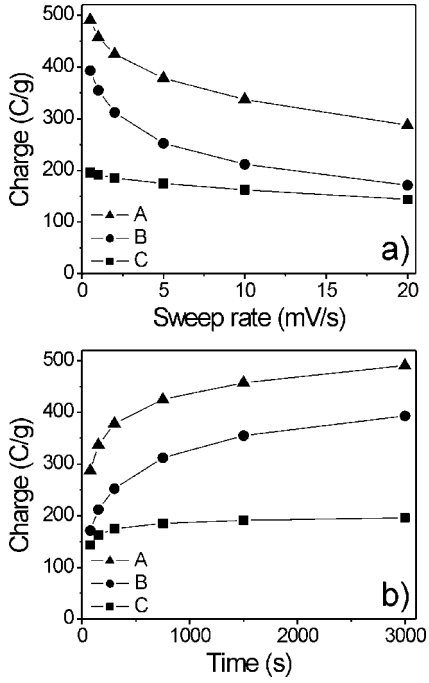

Figure 6. (a) Charge storage dependence on sweep rate. (b) Comparison of charging rates calculated from cyclic voltammetric data at various sweep rates. For both graphs, A and C refer to KLE-templated and untemplated nanocrystal films, respectively, while B refers to KLE-templated sol−gel films.

with the mole fraction of inserted lithium given by $x = QM/mF$. Here Q is the stored charge, M is the molecular weight, m is the mass, and F is the Faraday constant. The area under the CV curves represents the total amount of stored charge which arises from both faradaic and nonfaradaic processes. Note that for faster sweep rates, only the highest intensity part of the storage transient is collected and so larger peaks are observed. When the data are corrected for this effect, we find a steady decrease in charge storage with increasing rates. Figure 6a shows a direct comparison of the charge storage dependence on sweep rate in the range between 0.5 and 20 mV/s for the different titania systems discussed above. With decreasing sweep rate, the total amount of stored charge increases which indicates that full storage has not been achieved due to kinetic limitations associated with the diffusion of Li^+ through the anatase nanocrystals. The mole fraction of inserted lithium typically reaches a value of close to 0.5 when the anatase lattice is fully lithiated.[35−37] This corresponds to a specific charge capacity of 168 mAh/g.[35] At a sweep rate of 0.5 mV/s, the mole fraction of inserted lithium (cathodic process) was calculated to be 0.42 and 0.31 for the KLE-templated nanocrystal and sol−gel films, respectively. By contrast, nanocrystal films produced without any template displayed a much lower charge storage at the same sweep rate ($x = 0.18$). Significant differences in charging/discharging rates are also observed when comparing the templated nanocrystal films to the sol−gel-derived material. After a charging time of 150 s (see Figure 6b), the total charge stored in the KLE-templated nanocrystal films is about 340 C/g, i.e., almost 1.7 times higher compared to the highly ordered films (ca. 210 C/g) made from a sol−gel precursor.

Comparison of the templated films to the untemplated nanocrystal films clearly indicates that the introduction of interconnected porosity enhances the electrochemical charge/discharge properties by (1) minimizing solid-state diffusion path lengths and (2) facilitating mass transport of ions and solvent to the electrochemically active sites. Furthermore, the data reveal that a certain mesopore size is needed to allow for a reasonable molecular transport through the inorganic network. For this reason, both templated films feature significantly better electrochemical performance than untemplated nanocrystal films, indicating that the pores between the nanocrystals are not sufficiently large to allow solvent access to the bulk of the film. When comparing all three films, the total amount of charge stored in the KLE-templated nanocrystal films is highest and the charging/discharging rates are fastest, likely because the surface of the individual nanocrystal building blocks remains accessible to the electrolyte while the large pores provide a pathway for solvent diffusion through the film. In the case of the KLE-templated sol−gel films, the absence of bimodal porosity and the accompanied reduction in surface area impedes the insertion processes.

The total stored charge can be separated into three components: the faradaic contribution from the Li^+ insertion process, the faradaic contribution from the charge transfer process with surface atoms (referred to as pseudocapacitance),[9] and the nonfaradaic contribution from the double-layer effect. The latter two capacitive components can not be separated and were characterized by analyzing the CV data at various sweep rates according to

$$i = av^b \tag{2}$$

where the measured current i obeys a power law relationship with the sweep rate v.[37] Both a and b are adjustable parameters, with b-values determined from the slope of the plot of log i vs log v. There are two well-defined conditions, namely $b = 0.5$ and $b = 1.0$. For $b = 0.5$, the current is proportional to the square root of the sweep rate according to the following equation

$$i = nFAC^*D^{1/2}v^{1/2}(\alpha nF/RT)^{1/2}\pi^{1/2}\chi(bt) \tag{3}$$

where C^* is the surface concentration of the electrode material, α is the transfer coefficient, D is the chemical diffusion coefficient, n is the number of electrons involved in the electrode reaction, A is the surface area of the electrode materials, F is the Faraday constant, R is the molar gas constant, T is the temperature, and the function $\chi(bt)$ represents the normalized current for a totally irreversible system as indicated by the CV

(35) Jiang, C. H.; Wei, M. D.; Qi, Z. M.; Kudo, T.; Honma, I.; Zhou, H. S. *J. Power Sour.* **2007**, *166*, 239–243.

(36) Kavan, L.; Kalbac, M.; Zukalova, M.; Exnar, I.; Lorenzen, V.; Nesper, R.; Graetzel, M. *Chem. Mater.* **2004**, *16*, 477–485.

(37) Lindstrom, H.; Sodergren, S.; Solbrand, A.; Rensmo, H.; Hjelm, J.; Hagfeldt, A.; Lindquist, S. E. *J. Phys. Chem. B* **1997**, *101*, 7717–7722.

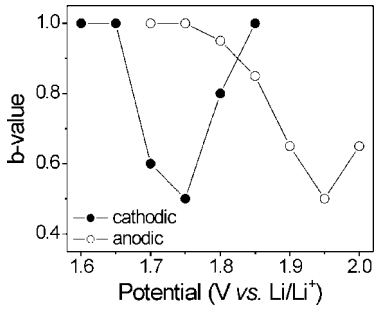

Figure 7. Calculated *b*-values for a KLE-templated nanocrystal film as a function of potential for the cathodic (Li^+ insertion) and anodic sweep (Li^+ extraction).

response.[38] The current response in eq 3 is assumed to be diffusion controlled, which is indicative of a faradaic insertion process.

The other well defined condition, $b = 1.0$, is representative of a capacitive response because the current is proportional to the sweep rate according to

$$i = vC_dA \tag{4}$$

where C_d is the capacitance.[37]

The calculated *b*-values for a KLE-templated nanocrystal film are shown in Figure 7. At the peak potentials of 1.75 and 1.95 V for cathodic and anodic processes, respectively, the *b*-values are close to 0.5. This shows that the currents arise primarily from the Li^+ insertion into the anatase lattice. At higher or lower potentials, however, the *b*-values are in the range of 0.8−1. This is, in turn, a good indication that the majority of the currents arise from capacitive effects. The fact that a large fraction of the current is capacitive in nature is in good agreement with our recent work on ultrathin nanoparticle films[11] and the work reported by Lindstrom el al.[37]

A closer examination of the voltammetric sweep rate dependence allows us to quantitatively distinguish the capacitive contribution to the current response. Using the concepts described above, we can express the current response at a fixed potential as being the combination of two separate mechanisms, namely surface capacitive effects and diffusion-controlled Li^+ insertion[39]

$$i(V) = k_1v + k_2v^{1/2} \tag{5}$$

For analytical purposes, we rearrange this slightly to

$$i(V)/v^{1/2} = k_1v^{1/2} + k_2 \tag{6}$$

In eq 5, k_1v and $k_2v^{1/2}$ correspond to the current contributions from surface capacitive effects and the diffusion controlled insertion processes, respectively. Plotting the sweep rate dependence of the current allows us to determine k_1 and k_2 from the slope and the *y*-axis intercept point of a straight line, respectively, at each fixed potential using eq 6. This methodology thus enables us to distinguish between the currents arising from Li^+ insertion and those from capacitive effects (details are described elsewhere).[11]

Figure 8 shows the total stored charge for a KLE-templated nanocrystal film, a KLE-templated titania film made from a sol−gel precursor (with dense walls rather than porous walls

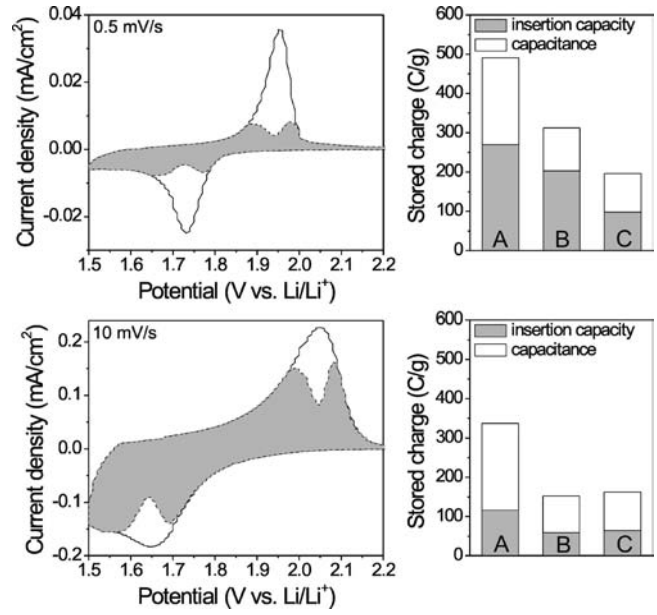

Figure 8. Left: cyclic voltammetric responses for KLE-templated nanocrystal TiO_2 at sweep rates of 0.5 (top) and 10 mV/s (bottom). The total current (solid line) is obtained experimentally. The capacitive current (shaded regions) is determined using eq 6. Right: corresponding comparison of the total stored charge. For both graphs, A and C refer to KLE-templated and untemplated nanocrystal films, respectively, while B refers to KLE-templated sol−gel films.

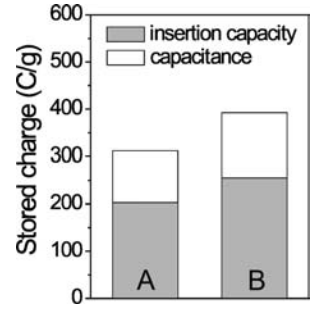

Figure 9. Comparison of the total charge stored in KLE-templated sol−gel TiO_2 thin films calcined at 600 (A) and 650 °C (B). The stored charge is divided into insertion capacity and capacitance. Films treated at temperatures at 650 °C show about a 20% increase in both insertion capacity and capacitance. As both films are close to 100% crystalline, we assign this increase to grain restructuring that opens up the necks in the cubic structure and enhances the interconnections between mesopores. That increased connectivity facilitates solvent diffusion through the film.

derived from the aggregation of nanocrystals), and for an untemplated nanocrystal film. The stored charge (gravimetrically normalized) is divided into insertion capacity and capacitive charge storage. For a relatively low sweep rate (0.5 mV/s, Figure 8), both types of templated mesoporous films feature much higher insertion capacities than untemplated nanocrystal films. This result indicates that the introduction of three-dimensionally interconnected mesoporosity significantly enhances the insertion processes by providing short diffusion path lengths and easy access for the electrolyte. Moreover, we find that for both of the nanocrystal-based materials, the total stored charge is about half-capacitive. By contrast, for the sol−gel material, only 1/3 of the stored charge is capacitive. The KLE-templated nanocrystal films thus show both the highest amounts of total stored charge and the highest capacitive charge storage. This is likely because the surface of the individual nanocrystal building blocks remains accessible to the electrolyte.

(38) Bard, A. J.; Faulkner, L. R. *Electrochemical Method: Fundamentals and Applications*; John Wiley and Sons; New York, 1980.
(39) Liu, T. C.; Pell, W. G.; Conway, B. E.; Roberson, S. L. *J. Electrochem. Soc.* **1998**, *145*, 1882–1888.

By comparison, both the capacitance and insertion capacity of the templated sol−gel films are lower, indicating that the reduction in surface area and the loss of the bimodal porosity both inhibit capacitive charge storage and impede insertion processes. Nonetheless, a thermal treatment of these sol−gel TiO_2 films at 650 °C leads to a rise in both by roughly 20% (Figure 9). We explain the increased insertion capacity and capacitance with the postulate that grain restructuring in the sol−gel derived material opens up the necks between cage pores and enhances the interconnectivity of mesopores[31] (we exclude a difference in crystallinity[40]). This, in turn, facilitates solvent diffusion through the film, a process that is needed for both insertion and capacitive charge storage. We find, however, that thermal processing can only be used to achieve a modest increase in capacitance in the templated sol−gel titania, as the walls are still fundamentally dense titania. No simple thermal processing step can be used to make these sol−gel-derived materials achieve the high surface area of the templated nanocrystal-based materials.

The untemplated nanocrystal films show much lower total charge storage. This is likely because the pores between the nanocrystals are not sufficiently large to allow solvent access to the bulk of the film and so only some fraction of the film near the liquid interface is electrochemically active. These films, however, possess fractional capacitive charge storage levels similar to the KLE-templated nanocrystal samples, which can be unambiguously attributed to the high surface area of a nanocrystal-based material.

The disparity in charge storage for different materials is even more pronounced at higher sweep rates (shown for 10 mV/s, Figure 8). The capacitive charge storage is basically unaffected by the increase in scan rate, while the insertion capacity drops significantly. The invariance of the capacitive values is due to the fast kinetics of both double-layer and pseudocapacitive processes. By contrast, the slow diffusion of lithium ions in TiO_2 (10^{-13}−10^{-17} cm^2/s)[11] results in a dramatic reduction in insertion capacity in data collected at a scan rate of 10 mV/s compared to data collected at 0.5 mV/s because there is simply less time for Li^+ to diffuse into the titania network. The first practical result from this is that the amounts of stored charge arising from capacitive effects are notably higher than those from Li^+ insertion. Second, the total stored charge of the templated nanocrystal films is nearly 2.5 times higher compared to templated sol−gel films. The electrochemical performance of the templated sol−gel films is now comparable to untemplated nanocrystal-based TiO_2 films. Overall, the results show again very clearly that templated nanocrystal architectures allow for high rate charging/discharging because 65% of the total stored charge is capacitive at a sweep rate of 10 mV/s.

In considering the implications of this work, some perspective is needed. A variety of studies have shown that creating nanoporous structures can increase capacity in both battery and capacitor materials. The purpose of this manuscript is not to be just another example of improved electrochemical capacity in a porous material.[2,4,6,7,11,41] Instead, our goal was to assess the parameters needed to systematically improve capacitive charge storage and to propose a nanoscale architecture that combines those key features. Moreover, we wanted an architecture that could be simply and generally produced using facile solution-phase assembly methods. The nanocrystal templating method described here shows just that combination of features. The method should be general to a broad range of nanocrystal systems with applications as cathodes, anodes, or double-layer capacitors.

More importantly, the design parameters described here provide a blueprint for future materials. As we have shown, mesoscale porosity is needed to allow facile electrolyte diffusion throughout the material. This is not sufficient for high capacitive charge storage, however, as the mesoporous materials described above with dense walls are fine battery materials, but unexceptional materials for applications as supercapacitors. For supercapacitors, we need much higher surface area and much smaller pores, like those formed in materials made of agglomerated nanocrystals.[11] In their pure form, these nanocrystal-based materials are also not ideal, however, as the electrolyte cannot effectively move through the small pores. The result, shown above, is a material with a high fractional capacitive charge storage, but a low overall capacity; presumably because the electrolyte can only penetrate a small fraction of the film. By employing a hierarchical architecture—that is first constructing nanocrystal building blocks and then assembling those into a mesoporous structure using surfactant templating—both the need for high surface area and the need for larger scale porosity to facilitate ion motion can be realized. As such, we feel that this work provides more than an example of a new high-capacity supercapacitor. It also proved a plan for the future construction of new battery and capacitor materials.

Conclusions

In this work, we show that considerable enhancement of the electrochemical properties of self-organized TiO_2 results when the films are both made from nanocrystals and mesoporous. Such materials show high levels of capacitive charge storage and high insertion capacities. When nanocrystal-based films are formed without mesoscale porosity, a high fraction of the total stored charge is again capacitive, but the total capacity is low, likely because most of the film is not accessible to the electrolyte/solvent. By contrast, when mesoscale porosity is created in a material with "dense" walls (rather than porous walls derived from the aggregation of nanocrystals), insertion capacities comparable to templated nanocrystal materials can be achieved, but the capacitance is much lower.

These results underscore the importance of pseudocapacitive behavior that develops in high surface area mesoporous oxide films. Moreover, the data suggest that both a mesoporous morphology and the use of nanocrystals as the basic building blocks are very promising for the rational development of metal oxide pseudo/supercapacitors. Through this combination, it may become possible to attain greater power densities while maintaining energy density in next-generation electrochemical capacitors that utilize this bimodal nanoporous architecture.

Acknowledgment. The authors thank Joe Nemanick, Erik Richman, Veronica Augustyn and Dina Fattakhova-Rohlfing for their contributions. This work was supported by the Office of Naval Research (B.D.) and by the National Science Foundation under Grant No. CHE-0527015 (S.H.T.). T.B. acknowledges the support of a DFG postdoctoral fellowship. Portions of this research were carried out at the Stanford Synchrotron Radiation Laboratory, a national user facility operated by Stanford University on behalf of the U.S. Department of Energy, Office of Basic Energy Sciences.

Supporting Information Available: TEM and XPS spectra. This material is available free of charge via the Internet at http://pubs.acs.org.

JA8057309

(40) Fattakhova Rohlfing, D.; Wark, M.; Smarsly, B.; Brezesinski, T.; Rathouský, J. *Adv. Func. Mater.* **2007**, *17*, 123–132.
(41) Long, J. W.; Dunn, B.; Rolison, D. R.; White, H. S. *Chem. Rev.* **2004**, *104*, 4463–4492.